Soils and Foundations 2014;54(3):296–312

The Japanese Geotechnical Society

Soils and Foundations

www.sciencedirect.com
journal homepage: www.elsevier.com/locate/sandf

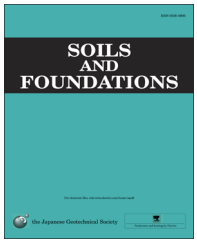

Understanding ground deformation mechanisms for multi-propped excavation in soft clay

S.Y. Lam*, S.K. Haigh, M.D. Bolton

Department of Engineering, University of Cambridge, UK

Received 30 June 2012; received in revised form 14 May 2013; accepted 8 April 2014
Available online 17 May 2014

Abstract

Deep excavation works are carried out to construct underground infrastructures such as deep basements, subways, and service tunnels. The execution of these deep excavation works requires the use of retaining walls and bracing systems. Inadequate support systems have always been of major concern, as excessive ground movement induced during excavation could cause damage to neighboring structures, resulting in delays, disputes, and cost overruns. To gain a better understanding of the mechanisms involved in soil excavations, centrifuge model tests of deep excavations in slightly over-consolidated soft clay have been carried out using a newly developed testing system, in which the construction sequence of a multi-propped wall for deep excavations can be simulated in flight. Deformation mechanisms are observed using Particle Image Velocimetry. Settlements of the ground surface and changes in pore water pressure are monitored during the excavation. The effects of prop stiffness, wall rigidity, and excavation geometry on the characteristics of ground deformation and soil–structure interaction are demonstrated and discussed. The use of the conservation of energy within the framework of the mobilizable strength design in calculating ground movements is validated and shown to perform satisfactorily.

Keywords: Centrifuge; Multi-propped excavation; Deformation mechanisms; Mobilizable strength design

1. Introduction

Deep excavations in soft clay are carried out for a variety of purposes, including the construction of station boxes and cut-and-cover tunnels during underground railway construction. In order to prevent the collapse of these excavations and to minimize the disruption to neighboring infrastructures due to settlements, multiple levels of props are used to support the retaining walls during construction. In order to better understand the mechanisms involved in the construction of multi-propped deep excavations in soft clay, centrifuge model tests have been carried out using a newly developed testing system, in which the construction sequence of a multi-propped deep excavation can be properly simulated (Lam et al., 2012).

2. Methodology

Small-scale centrifuge models can be used to simulate the prototype behavior of an excavation in soft soil. A

*Correspondence to: Advanced Geomechanics, Pty. Ltd. 52-54, Monash Ave, Nedlands, WA 6009, Australia.

Peer review under responsibility of The Japanese Geotechnical Society.

Production and hosting by Elsevier

http://dx.doi.org/10.1016/j.sandf.2014.04.005

centrifugal acceleration field of 60 g is used in a small-scale model to match the stress induced by gravity in the prototype. The principal challenge is to design a test package that can simulate the construction sequence of a propped excavation in the field, so that a cross-section can be used for the measurement of the resulting ground movements. The advantages are that the tests can be repeated with planned variations, and that the model can be observed continuously from the occurrence of small deformations up to complete collapse, which is not generally possible in the field. Similar approaches were adopted by Takemura et al. (1999) and Loh et al. (1998).

Table 1
Summary of centrifuge testing program.

Centrifuge tests	1	2	3	4	5
	Floating rigid wall with stiff props	Floating flexible wall with stiff props	Fixed-base flexible wall with base grout	Floating rigid wall with soft props	Fixed-base flexible wall in shallow clay
Objectives	Baseline test	Wall stiffness	Fixed-wall toe condition	Prop stiffness	Clay thickness
Depth of clay stratum, D (mm)	300	300	300	300	160
Prop stiffness (kN/mm)	1.66	1.66	1.66	0.55	1.66
System stiffness $EI/\gamma_w s^4$	2860	106	106	2860	106
Toe fixity	Free	Free	Fixed	Free	Free

Note: Numbers are in model scale.

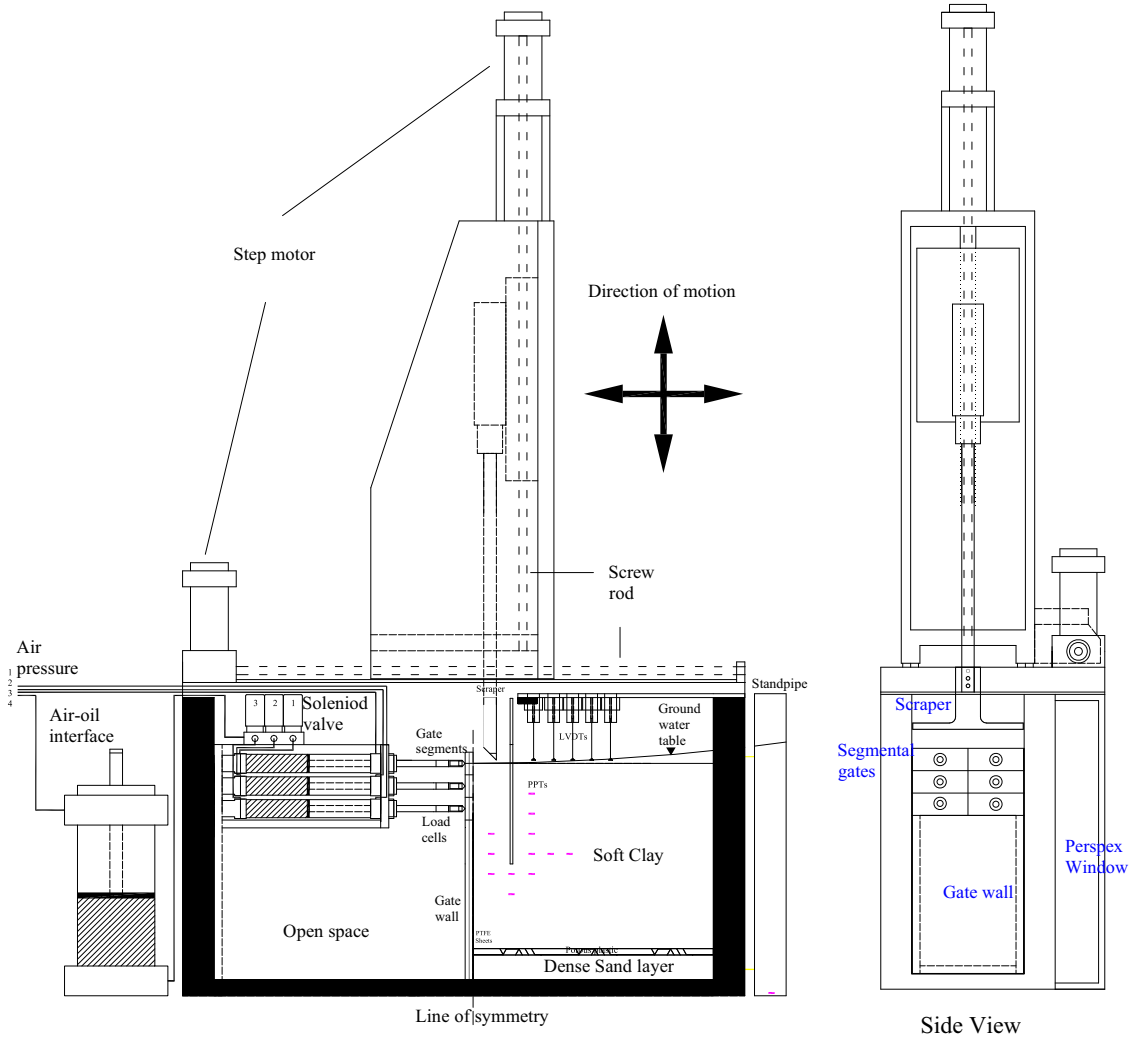

Fig. 1. Schematic diagram of experimental setup with in-flight excavator.

3. Test program

Five centrifuge model tests were carried out in order to study the undrained short-term behavior of excavations in soft clays. Test 1 investigated the behavior of a floating rigid wall supported by stiff props; Test 2 studied the effect of wall flexibility on the deformation mechanism; Test 3 looked into the effects of a grout layer fixing the wall toe; Test 4 simulated a rigid wall supported by soft props to study the effect of soft propping on changes in the deformation pattern; Test 5 studied the case of an excavation in shallow clay using a flexible wall. A summary of the test program is given in Table 1.

4. Experimental setup

Fig. 1 shows the experimental setup. The rectangular model container is made of an aluminum alloy with internal dimensions 790 mm × 180 mm × 470 mm. The front face of the container consists of a Perspex window, which enables the testing process to be monitored by cameras. The back of the container contains holes to allow for both the installation of pore pressure transducers and drainage.

The model consists of a base layer of dense fine fraction *E* sand, formed by pluviation using an automatic pouring machine (Madabhushi et al., 2006). The properties of the sand are shown in Table 2. Overlying the sand is a layer of lightly over-consolidated kaolin clay. A standard procedure was adopted to ensure the reproducibility of the strength profiles in each test. Speswhite kaolin clay, whose properties are given in Table 3, was mixed from powder to about twice the liquid limit (120% moisture content), the mixing taking place under a vacuum for at least 2 h. The inner surface of the test container was coated with silicone grease to minimize friction against the clay, and the slurry was carefully placed onto the sand layer to a height of 550 mm, with infiltration being prevented by a sheet of filter paper. A piston was then placed on the surface of the clay, and the container was placed in a hydraulic press. Pressure was applied in loading steps to prevent immature bearing capacity failure. The final pressure of 160 kPa was intended to achieve an undrained strength of 25 kPa for the clay at mid-depth when it had swollen back into equilibrium at 60 g.

Table 2
Properties of fraction *E* sand (Haigh and Madabhushi, 2002).

Properties	Value
Minimum void ratio	0.613
Maximum void ratio	1.014
Minimum dry unit weight	12.9 kN/m^3
Maximum dry unit weight	16.1 kN/m^3
Specific gravity of solids	2.65
D_{10}	95 μm
D_{50}	140 μm
D_{90}	150 μm

Table 3
Mineralogy and properties of Speswhite Kaolin.

Mineralogy/properties	Value
SiO_2	47%
Al_2O_3	38%
300 Mesh residue	0.02% maximum
≥ 10 mm	0.5% maximum
≤ 2μm	80 ± 3%
Specific gravity	2.6
Surface area	14 m^2/g
pH	5.0 ± 0.5
Oil absorption	42 g/100 g
Water soluble salt content	0.2%

Prior to the final loading step, the clay was unloaded and nine PPTs were inserted through the pre-drilled openings on the back wall of the container. PPTs were installed through 90-mm-long holes augured horizontally into the clay using a hand drill. Unconsolidated slurry was then injected to fill the holes, and the openings were sealed. The final locations of the PPTs are shown in Fig. 2. After the installation of the PPTs, the pressure was returned to 80 kPa, and after equilibration, the consolidation pressure was further increased to 160 kPa.

Prior to testing, the pressure was reduced to 80 kPa and the clay was allowed to swell. Removal of this final pressure was known to be possible without drawing air into the clay. The front wall of the model container was then removed and the clay was trimmed to height with spaces cut for installation of the prop system and the retaining wall. An O-ring seal was placed along the edges of the gate wall to seal the gaps on the side walls of the box. The retaining wall was made of either a 2-mm- or a 6-mm-thick aluminum alloy plate with a stiffness (*EI*) of either 10.4 MNm^2/m or 280.8 MNm^2/m at the prototype scale, respectively. These walls simulate a sheet pile wall (US steel, PDA-27) and a 0.9-m-thick diaphragm wall in the field, respectively.

Greased wiper seals were used to prevent water from seeping past the sides of the wall and to ensure a free sliding condition with minimal friction. The wall was installed at a depth of 160 mm (9.6 m at the prototype scale).

With the clay cross-section uppermost, grains of black-dyed fraction E sand were blown onto the clay to provide texture to ensure good tracking using PIV. Lubricant was then applied to the Perspex window to reduce friction against the soil cross-section. The hollow frame, Perspex window, and window frame were then bolted to the main body of the container.

In order to validate the PIV results, LVDTs were placed to measure the soil settlement profile. A laser sensor was used to monitor the lateral displacement at the top of the wall. Finally, the water table in the clay was maintained at the ground surface by permitting overflow from a stand pipe, which would be supplied continuously throughout the experiment. Two 8-megapixel cameras took pictures throughout the experiment with the provision of suitable lighting. The instrumentation layout is shown in Fig. 2.

A two-axis servo actuator (Lam et al., 2012) was used to excavate the clay. The servo actuator was mounted above the model container and moved a T-shaped scraper in order to perform in-flight excavation at 60 g. Instruments comprising pore pressure transducers in the soil, earth pressure cells on the

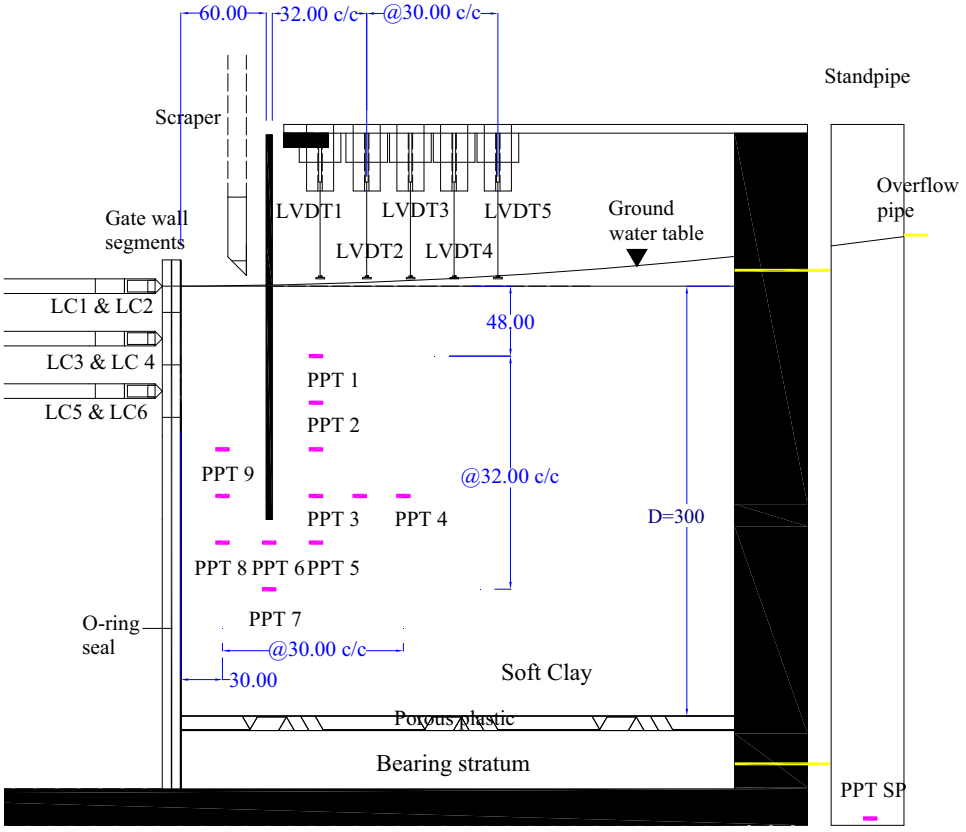

Fig. 2. Positions of instruments on model package in elevation view (in mm).

retaining wall, bending moment strain gauges on the wall, load cells on the props, and linear variable transformers for displacement measurements were installed. Digital cameras were mounted in front of the Perspex window and LED arrays were situated to illuminate the clay cross-section without causing glare or shadows.

The vertical plane through the center of an excavation can be regarded as a plane of symmetry. A "gate wall" (as shown in Fig. 1) represents this plane of symmetry and the centerline of the excavation pit, such that only one side of the excavation needs be modeled. Low friction material PTFE sheets (an interface friction angle, δ, of less than 2.5°) were glued onto the gate wall in order to minimize the vertical friction, and steps were also taken to prevent its lateral movement prior to excavation. Three pairs of cylinders (Festo DSNU 25-125) were mounted on a rigid support frame and positioned at 0 mm, 36 mm, and 72 mm below the initial clay surface to provide in-flight support during the experiment, initially to the gate wall and ultimately to the retaining wall.

Props were driven in the cylinders via pistons which were actuated through a hydraulic/pneumatic control system, as described in Lam et al. (2012). Before the experiment, the system was saturated with hydraulic oil. The compressibility of silicone oil of a volume of 100 mm^2 at room temperature is less than 0.1% at 1 MPa. The prop stiffness was obtained by conducting load displacement tests on each prop. The target stiffness of a fully-saturated prop was found to be about 1.66 kN/mm in model scale.

Fig. 3 shows the gate system. At the start of the experiment, three pairs of sacrificial gates, each 36 mm high, are located on the top of the gate wall. Their purpose is to support and retain the soil to be excavated. The gates are temporarily supported by the pairs of cylinders as the soil reconsolidates prior to excavation. The forces required to support the gate segments are monitored by axial load cells attached at the end of each prop. Fig. 3 shows the sequence of the first excavation stage. At the start of the excavation, the first pair of cylinders is retracted so that the first layer of gates is in an unstable condition and is easily knocked down by the scraper of the in-flight excavator. The in-flight excavator then makes a 4-mm cut into the soil, which is scraped off into the open space inside the cylinder support system. The scraper then returns to its initial position and makes another 4-mm cut, repeating this until the excavation level reaches the top of the second level of gates. At that moment, the first level of props is advanced to support the retaining wall. The required prop force can be adjusted based on the prop load cells. This completes the first stage of the excavation. As the scraper has an inverted T-shape, it can continue scraping below the first pair of props. The second and third stages of the excavation can therefore proceed by repeating the same steps carried out for the first level. For a higher level of experimental details, readers may refer to Lam et al. (2012) and Lam (2010).

5. Soil properties

Consolidated undrained triaxial compression tests were carried out to characterize the undrained shear strength of the soil. The averaged undrained shear strength was found to be

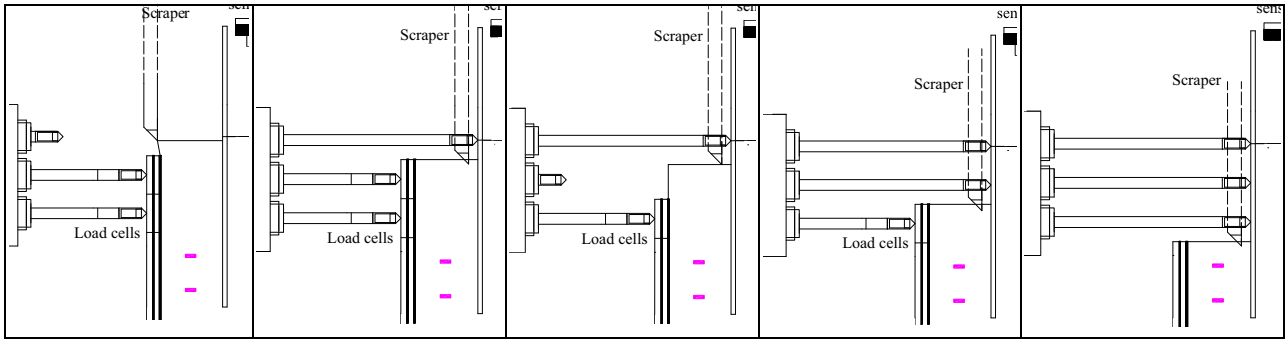

Fig. 3. Excavation sequences: segmental length = 36 mm.

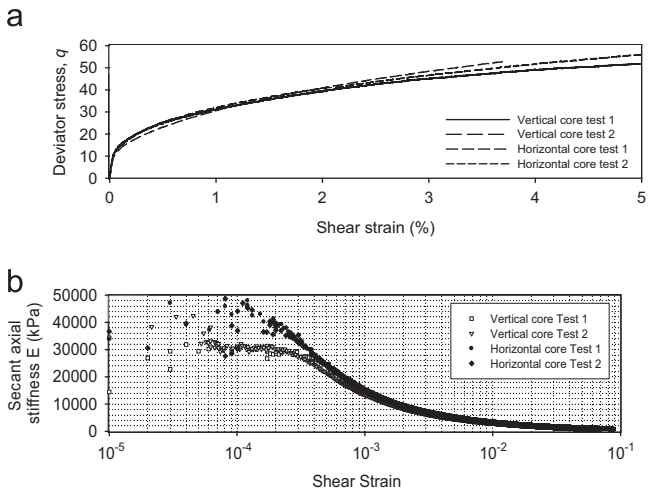

Fig. 4. (a) Stress strain and (b) stiffness degradation curves for vertically and horizontally cored samples at mid-depth of soft clay ($p_0' = 125$ kPa; $p' = 26$ kPa).

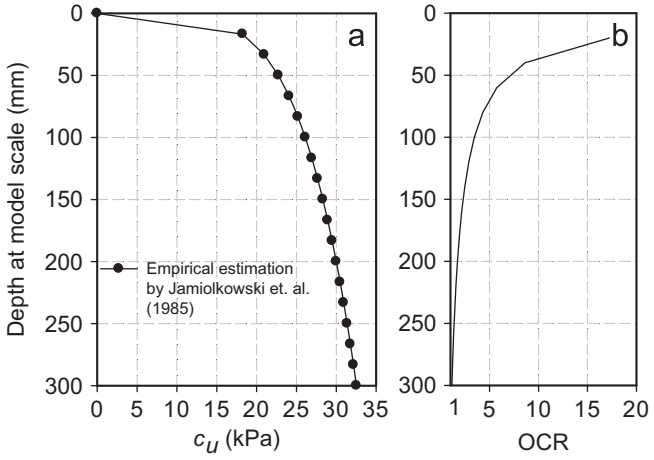

Fig. 5. (a) Undrained shear strength and (b) over-consolidation profile at 60 g.

25.5 kPa, as shown in Fig. 4. In Fig. 5, an estimated profile with the empirical relation suggested by Jamiolkowski et al. (1985) is shown for comparison.

Jamiolkowski et al. (1985) related the strength of the soil to the vertical effective stress and over-consolidation ratio using

$$c_u = 0.22\sigma_v'(OCR)^{0.8} \quad (1)$$

In the present study, the stress strain behavior of lightly over-consolidated Speswhite kaolin at small and intermediate strain levels was studied using a new local strain measurement and dynamic wave propagation system incorporated into a triaxial apparatus. Isotropically consolidated compression tests were carried out on two vertically and two horizontally cut cylindrical specimens, 100 mm by 50 mm, taken from a block of clay pre-consolidated at 160 kPa. All specimens were isotropically consolidated to 125 kPa and then allowed to swell back to 26 kPa before application of the deviatoric load, in order to replicate the mean stress at the mid-depth of the wall. Compressive strain was applied over 8 h at a rate of 0.16 mm/h. Secant Young's modulus was calculated as the ratio of the deviator stress to the locally measured axial strain. Subsequently, the undrained shear modulus was derived by assuming a Poisson's ratio of 0.5. The secant axial modulus was plotted against local strain on a semi-log scale for the purpose of investigating the stiffness degradation in the very small to finite strain range. As observed in the stress–strain curves and stiffness degradation curves shown in Fig. 4, the horizontally cut specimens are slightly stiffer and stronger than the vertically cut specimens. This could be ascribed to the direction of the bedding plane of the clay particles forming during the deposition and the one-dimensional consolidation.

Shear wave velocity was measured using bender elements within the samples. By sending shear waves with a high frequency of 1 kHz, the difference between the arrival time and the input signal can be assessed by the cross-correlation method. The sample length to wavelength ratio was chosen to be 9.6 in order to separate the near-field coupled compression and the shear waves, hence avoiding near-field effects (Leong et al., 2005).

From the shear wave velocity, shear stiffness G_o can be determined from the elastic wave propagation theory as follows:

$$G_o = \rho V_s^2 \quad (2)$$

where ρ is the total density of the soil.

Three bender element tests were carried out on one vertical and two horizontal core samples. The maximum shear stiffness

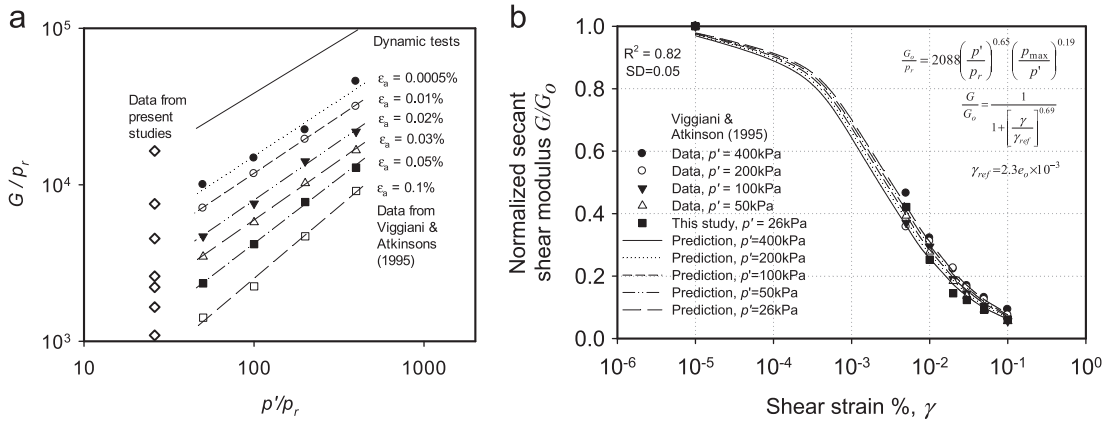

Fig. 6. Variation in measured and predicted shear modulus (G) with mean stress and shear strain from triaxial tests in (a) G/p_r vs p'/p_r space and (b) G/G_o vs γ space.

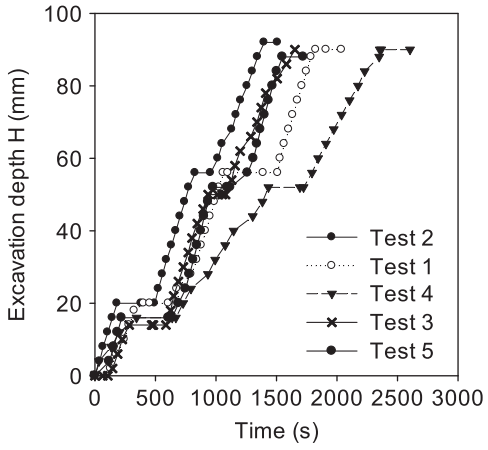

Fig. 7. Progress of excavation.

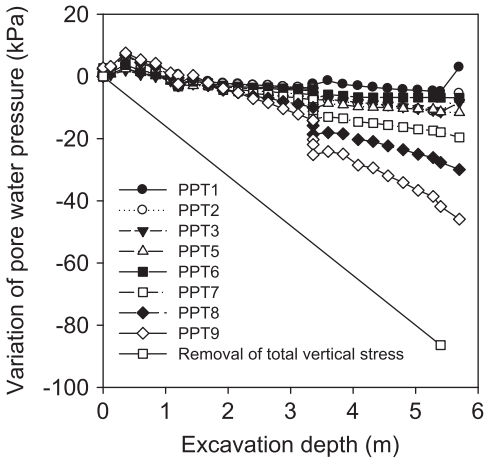

Fig. 8. Variation in excess pore water pressure during excavation with stiff props and wall (Test 1).

levels of the vertically and horizontally cored samples were found to be 16 MPa and 18 MPa, respectively.

The test results at a low confining stress were plotted together with the relationship of Viggiani and Atkinson (1995) at a medium confining stress in logarithmic G_o/p_r and p'/p_r space at different strain levels, as shown in Fig. 6(a), where p_r is a reference pressure taken to be 1 kPa. The data point on the plot fell close to the straight line given by Eq. (3), namely,

$$\frac{G_o}{p_r} = A\left(\frac{p'}{p_r}\right)^n \left(\frac{p_{max}}{p'}\right)^m \tag{3}$$

where A, n, and m are non-dimensional parameters with values of 2088, 0.653, and 0.194, respectively. For the present study, the value of G_o calculated by applying Eq. (3) was found to be 22 MPa. The measured values obtained from bender element tests were within 20% of this prediction.

A hyperbolic function is introduced to relate secant shear modulus with G_o, shear strain γ, and reference strain γ_{ref}. Reference strain γ_{ref} was assumed to be a linear function of void ratio e_o, following Vardanega (2012). Using the least squares method, the coefficient of correlation was found to be 0.82. Parameters a and b in Eqs. (4) and (5) were found to be 0.69 and 2.3, respectively. The correlation is plotted together with the actual measurements in Fig. 6(b).

$$\frac{G}{G_o} = \frac{1}{1+[\gamma/\gamma_{ref}]^a} \tag{4}$$

$$\gamma_{ref} = be_o \times 10^{-3} \tag{5}$$

6. Excavation test procedures

The in-flight excavator was bolted above the model container, and the integrated assembly was transferred onto the centrifuge swing platform and brought to its scale acceleration of 60 g. There are three test phases for a typical centrifuge test of a deep excavation–reconsolidation, in-flight excavation, and long-term equilibration.

As an increase in soil self-weight leads to an increase in excess pore pressure, the model ground was allowed to

undergo 5 h of reconsolidation to achieve at least 90% of the consequential consolidation prior to the excavation.

In order to ensure that realistic quasi-undrained responses are observed, the excavation process should be finished within a reasonably short period of time. Fig. 7 shows the progress of the excavation in all tests. The excavation to a depth of 5.5 m was finished within 30–40 min (72–96 days at prototype scale), which is similar to the rate of the excavation in the field.

Following the excavation, the test was allowed to continue and excess pore pressures were observed to dissipate as long-term deformations were monitored. In the following section, short-term ground deformation data of the tests are presented.

7. Pore pressure response

As the excavation proceeds, the ground water level inside the excavation falls simultaneously, remaining coincident with the excavation level, a standpipe maintains the water table at the ground surface outside the excavation throughout the test. Under such conditions, downward seepage at the backside of the wall and upward seepage in front of the wall should be expected. Fig. 8 shows the variation in pore water pressure during the excavation in Test 1 using a 0.9-m-thick diaphragm wall. In front of the wall, there was negative pore pressure (PPT 9 and PPT 8) due to the reduction in total mean stress during the excavation. The magnitude of negative pore pressure was smaller than the effective over-burden pressure lost in the excavation. This is due to the fact that the negative pore pressure was canceled out by the positive pore pressure generated by shear deformation of the clay. On the other hand, the change in pore pressure measured at the back of the retaining wall (PPT 1, PPT 2, and PPT 3) was relatively small, because the stiff prop supports limited the lateral wall deformation, and thus, limited any reduction in lateral horizontal stress.

8. Ground settlement and wall deflection

The wall deflection and the ground settlement profile during the undrained excavation are vital parameters for assessing the potential damage to neighboring structures and buried services. In an ideal excavation process, the support level is installed at an early stage in order to minimize cantilever movement of the wall. However, this may not be possible in practice due to a variety of site constraints and construction sequences. In the present study, the excavation procedure was initiated with the cantilever stage of excavation, which was then followed by the singly-propped excavation, and finally the multi-propped excavation. Ground movements were captured using PIV (White et al., 2003). The ground settlement profile at discrete points, monitored using LVDTs, is also included for comparison for Test 2. In general, the results obtained by the LVDTs and the PIV technique are comparable, which verifies that the model is tested under plane strain conditions.

Fig. 9 shows the development of lateral wall displacement and ground settlement during the excavation behind a flexible wall (Test 2). Consistent with the results shown by previous

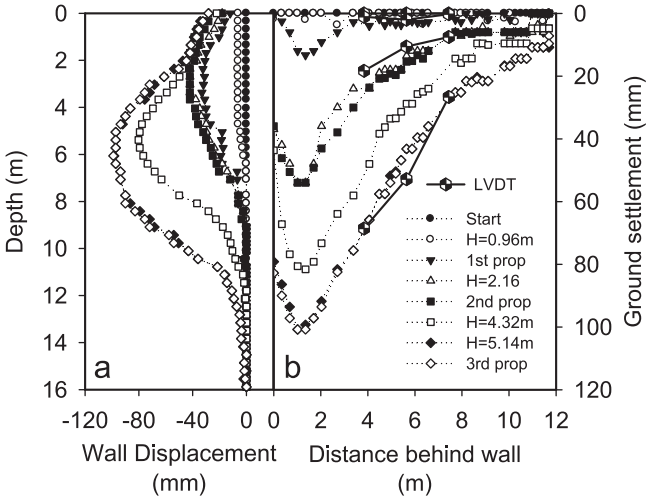

Fig. 9. Development of (a) wall deformation and (b) ground settlement with progress of excavation (Test 2).

researchers (i.e., Powrie, 1986), the rotation of the wall about its toe was observed during the cantilever excavation stage. A maximum incremental cantilever wall deflection of about 10 mm at prototype scale (Fig. 9(a)) was observed at the wall crest, equivalent to 0.2% average engineering shear strain in the 45 degree triangular zone behind the wall, following Osman and Bolton (2004).

When considering the incremental deformations of a multi-propped wall supporting a deep excavation in soft, undrained clay, at each stage of excavation, the incremental displacement profile of the ground and the wall below the lowest prop was assumed by O'Rourke (1993) to be a cosine function, namely,

$$\delta w = \frac{\delta w_{max}}{2}\left(1 - \cos\left(\frac{2\pi y}{\lambda}\right)\right) \quad (6)$$

where δw is the incremental wall displacement at any distance y below the lowest support, δw_{max} is its maximum value, and λ is the wavelength of the deformation, regarded as being proportional to the length s of the wall below the lowest level of current support $\lambda = \alpha s$.

O'Rourke (1993) defined the wavelength of the deformation as the distance from the lowest support level to the fixed base of the wall. Osman and Bolton (2006) suggested an expression for the wavelength of the deformation based on the wall end fixity. For walls embedded into a stiff layer beneath the soft clay, such that the wall tip is fully fixed in position and direction, the wavelength was set to be equal to the wall length ($\alpha = 1$). For short walls embedded in deep soft clay, the maximum wall displacement occurs at the tip of the wall so the wavelength was taken as twice the projecting wall length ($\alpha = 2$). Intermediate cases were described as restrained-end walls ($1 < \alpha < 2$). For excavations in deep soft clay layers, the α value is found to be 1.3–1.5. It should be noted that this value would be a function of the soil-wall relative stiffness.

The maximum settlement occurs some distance away from the wall, unlike the triangular trough observed by Powrie (1986). The subsequent stages of excavation involve a deep-seated soil flow mechanism and bulging of the retaining wall

below the lowest level of struts (Fig. 9(b)). The maximum incremental lateral wall displacements for the second and third stages were 30 mm and 90 mm, respectively. These movements were equivalent to about 0.6% and 1.5% of the average incremental engineering shear strain, respectively, within the deformation zone, according to Bolton et al. (2008).

These findings once again show the importance of the small strain stiffness of over-consolidated soil in the analysis of multi-propped excavations. The development of settlement troughs is complicated by the superposition of deep and shallow mechanisms at different points during the excavation process. This observation is consistent with the general observation given by Clough and O'Rourke (1990) that the settlement trough of a multi-propped excavation is bounded by a trapezoidal zone extending up to 2 times the maximum excavation depth back from the wall.

9. Effect of depth to stiff bearing stratum

Mana and Clough (1981) presented parametric studies on the effect of the depth to the bearing stratum on maximum lateral wall displacement for a fixed base wall. The results showed that movements increase with both excavation width and depth to the bearing stratum, the lateral wall displacements increasing by a factor of 1.5 when the depth to the stiff layer doubled. In this analysis, however, soils are considered to be elastic, implying that the development of plastic strain is not possible, hence over-predicting the soil movements.

Jen (1998) investigated the same issue with a more sophisticated numerical constitutive model, (MIT-E3). Parametric studies on the effect of the depth to the hard stratum using a floating wall were carried out. Results show that the depth only affects the wall deflection below the excavation level, especially near the wall toe. On the other hand, the behavior of shallower clay has a stronger impact on the distribution of far-field ground settlement. As the location of the rigid base becomes shallower, the settlement trough tapers off more rapidly. The width of the settlement trough is approximately equal to the depth of the stiff stratum.

Fig. 10 shows the development of wall displacement and ground settlement as the excavation in shallow clay progresses (Test 5). Since the wall toe is not fixed at the base, toe rotation and wall bulging are the major deformation modes. The lateral wall deformation shape is very similar to that of Test 2, except that the length of the bulge is limited to the depth of the stiff layer.

The evolution of the soil displacement mechanism is illustrated in Fig. 11 at different stages of excavation. The introduction of the first pair of pre-loaded props induces inward displacement at the wall crest (as shown in Fig. 11 (a)). Beyond this stage, the deformation mechanism changed to a free bulging mode, equivalent to loading a vertical simply-supported beam. The majority of the wall rotation is developed at this stage since there is no rotational restraint at the wall crest (as shown in Fig. 11(b)). After the introduction of the second row of props, the wall length below the lowest prop is restrained from rotating at the prop location. The maximum

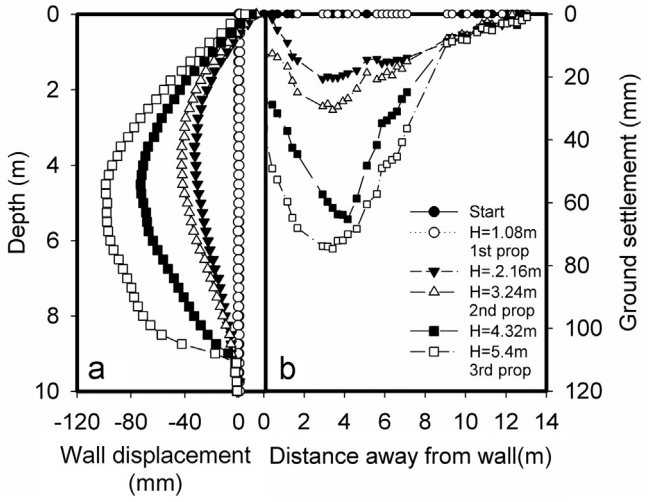

Fig. 10. Development of (a) wall deformation and (b) ground settlement with progress of excavation (Test 5).

lateral wall displacement during the second and third stages were 45 mm and 100 mm, respectively. These movements were equivalent to about 0.9% and 2% of the average overall engineering shear strain, respectively, within the deformation zone according to Bolton et al. (2008).

The maximum wall displacement is not affected by the depth to the stiff stratum. The difference between the two tests is about 10%. This is comparable to the observation from the numerical simulation of Jen (1998), who suggested that the maximum wall movement would differ only by 20% when the depth of stiff layer increased from 5 m to 50 m below the wall toe. The settlement trough is narrower when the soft clay layer is shallow, owing to the improved fixity at the wall base. This observation echoes the results simulated using FEA by Jen (1998). This implies that an engineer who wants to control the extent of the excavation-induced movement should consider improving the fixity at the wall toe with ground-improvement methods.

10. Effect of wall toe fixity conditions

For a deep excavation in a soft ground, the maximum wall deflection usually occurs at the final excavation level. To limit the wall deflection at this level, ground improvement techniques such as jet-grouting are usually employed prior to the excavation. A common approach is to improve the entire soil layer within the excavation zone below the excavation level to fix the wall toe. In the present study, a centrifuge test (Test 3) was carried out to understand how an infinitely stiff fixed-base grout layer at the wall toe would affect the deformation mechanism.

Fig. 12 shows the variation in wall displacement and ground settlement for an excavation using a fixed-based wall (Test 3). Since the wall toe is fixed, only wall bulging movement is possible. The lateral wall deformation mode shape is similar to that of Test 2, except that a rotational restraint is imposed at the wall toe. Fig. 12 shows the deformation of a fixed-base

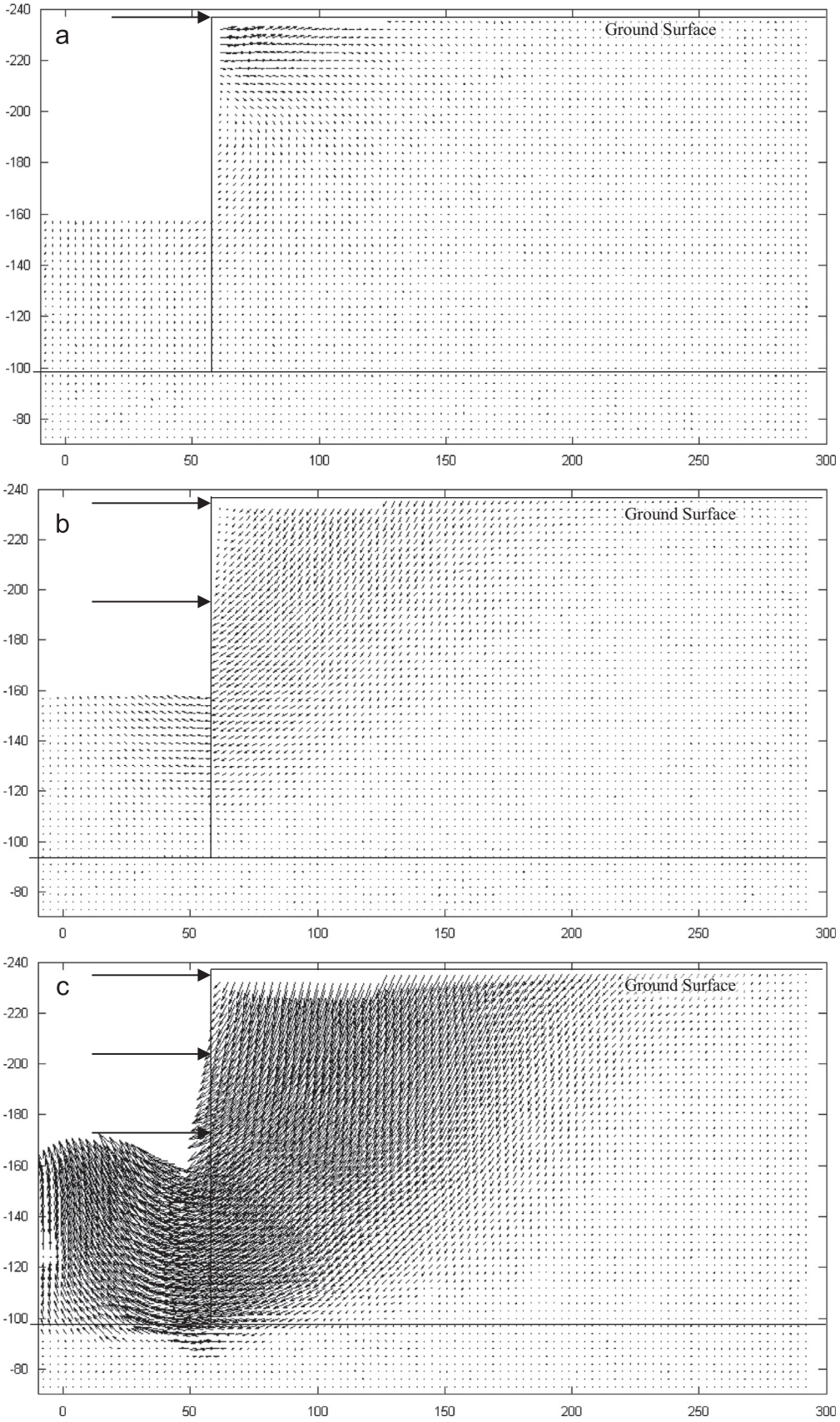

Fig. 11. Incremental displacements for different stages of excavation for Test 5.

retaining wall for an excavation depth of 5.4 m. The maximum lateral wall displacements for the second and third stages were 40 mm and 65 mm, respectively. These movements were equivalent to about 0.8% and 1.3%, respectively, of the average overall engineering shear strain within the deformation zone. In effect, the wall toe fixity controlled the lateral soil deformation below the final excavation level. A reduction of 50% in lateral wall movement for flexible retaining structures can be achieved by fixing the wall toe.

Following the approach of Clough et al. (1989), the wall displacement can be represented by a normalized wall displacement and depth below the lowest prop normalized by a wavelength of deformation, as shown in Fig. 13. Results show that the normalized curves for both floating and fixed-base walls broadly follow the cosine curves. The deformation shape is a good representation of a typical wall bulging displacement profile below the lowest prop for multi-prop excavation stages. The wavelength of the deformation is a function of the depth to the stiff layer. For a fixed based wall, the wavelength is the same as the unsupported length of the wall below the lowest prop, whereas the wavelength for a floating wall is 1.3–1.5 times the unsupported length of the wall below the lowest prop. A simplified deformation mechanism for a narrow excavation is suggested by Lam and Bolton (2011), as shown in Fig. 13. This mechanism of shearing at constant volume consists of three zones of distributed shear and generally represents a continuous and compatible flow of soils with no relative sliding at the boundaries. Along the dashed flow lines, the displacement is described by Eq. (6).

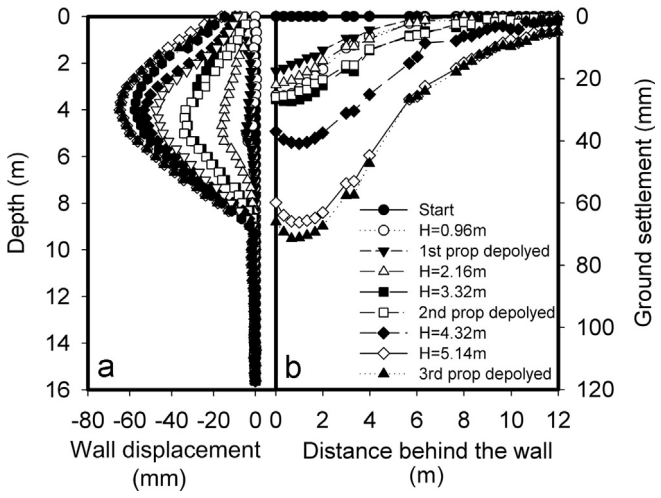

Fig. 12. Development of (a) wall deformation and (b) ground settlement with progress of excavation (Test 3).

11. Effect of wall stiffness

Fig. 14 shows the variation in wall displacement and ground settlement for an excavation using a floating rigid diaphragm wall as the digging progresses (Test 1). Clough et al. (1989) proposed a semi-empirical procedure for estimating the movement of excavations in clay in which the maximum lateral wall movement, δ_{hm}, is evaluated relative to the factor of safety (FS) and system stiffness η, defined as

$$\eta = EI/\gamma_w h^4. \tag{7}$$

where EI is the flexural rigidity per unit width of the retaining wall, γ_w is the unit weight of water, and h is the average support spacing.

The variation in maximum normalized measured lateral displacement (w_{max}/H) with system stiffness is shown in Fig. 15. A worldwide database of excavation case histories in soft clays ($c_u < 75$ kPa), as reported in Lam and Bolton (2011), is also included for reference. Lam and Bolton (2011) showed that the normalized lateral wall displacement decreases with an increasing factor of safety. There is no simple dependence, however, of normalized wall displacement on the factor of safety. Similar observations can be made from centrifuge data. A large amount of scatter can be seen in the data from walls with similar factors of safety and system

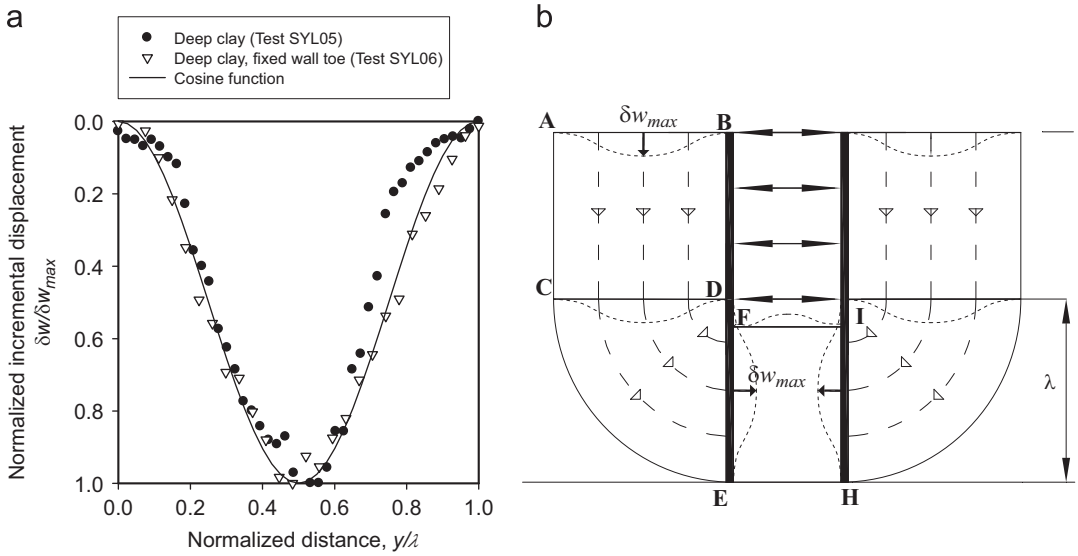

Fig. 13. Variation in (a) normalized incremental displacement with distance below the lowest prop and (b) simplified deformation mechanism.

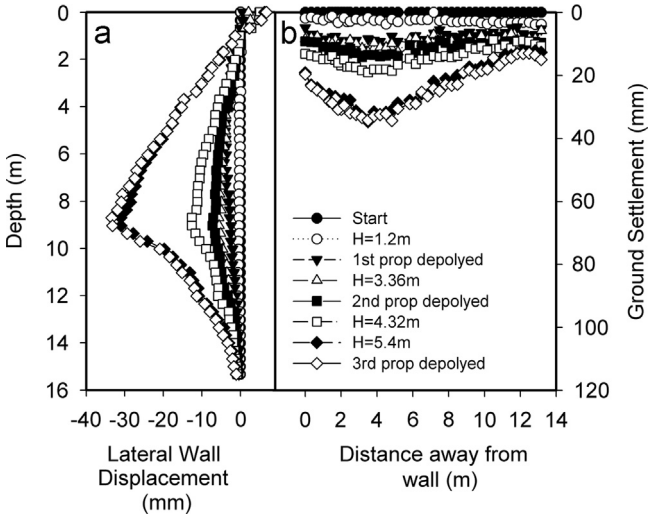

Fig. 14. Development of wall deformation and ground settlement with progress of excavation (Test 1).

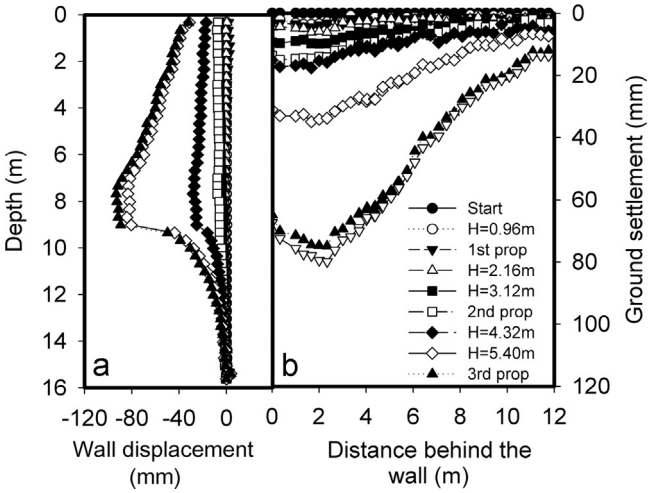

Fig. 16. Development of wall deformation and ground settlement with progress of excavation (Test 4).

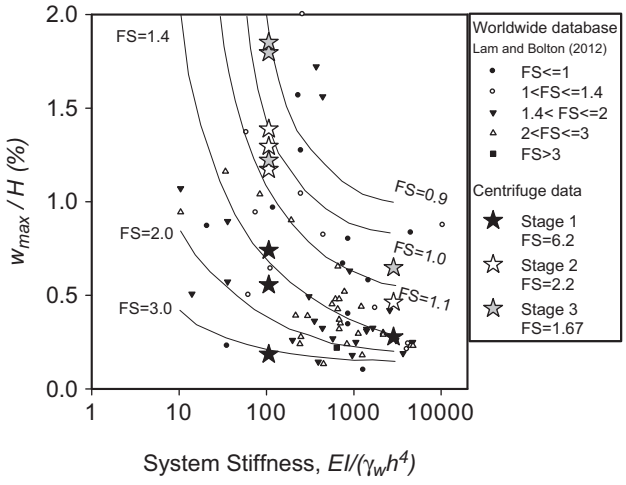

Fig. 15. Variation in maximum horizontal wall displacement with system stiffness defined by Clough et al. (1989) and factor of safety against base heave.

stiffness at the same stage of excavation. This could be due to the fact that using factors of safety to quantify wall deformation means ignoring the small strain stiffness of the soil, the incremental nature of the construction, and most importantly the size of the deformation mechanism quantified by the wavelength of the deformation mechanism, i.e., λ in Eq. (6).

12. Effect of soft props

According to Jen (1998), reductions in strut stiffness cause increases in the wall deflection occurring above the excavation grade, with the maximum wall deflection occurring closer to the excavated level, while the lateral soil movement below the excavation level is not influenced by the stiffness of the prop system. As the props become more compressible, the maximum wall movement increases with negligible movement of the settlement trough position. The reduction in prop stiffness also causes the soil to develop a shallower failure mechanism. A centrifuge experiment (Test 4) was carried out to investigate this issue. The prop stiffness is obtained by conducting axial-load displacement tests in a loading rig. The target stiffness of a fully-saturated prop is found to be about 1660 N/mm in model scale. For the present test, the prop stiffness is adjusted to be 550 N/mm in model scale. Fig. 16 shows the development of wall deformation and ground settlement with the progress of the excavation. The lateral wall deformation shape is very similar to that of Test 1, except for the fact that the soft prop response allows the rigid body displacement of the retaining wall into the excavation pit. Fig. 16 shows the total deformation mechanism for the test. A triangular wedge mechanism is found to be the major mechanism on the active side. The maximum lateral wall displacement for the second and third stages were 37 mm and 80 mm, respectively. These movements were equivalent to about 0.74% and 1.6%, respectively, of the average overall engineering shear strain, within the deformation zone. Since the soft response of the props allows a rigid body lateral displacement of the wall, soil on the active side is being sheared at an angle of 45°. A settlement profile with the same width of the length of the wall is induced. This extra soil strain developed on the active side may have induced the strain-dependent degradation of the soil stiffness causing more soil deformation as the excavation depth goes deeper.

13. Soil strains

This section presents the engineering shear strain distributions within the soil during the excavation process. Strains are calculated based on the PIV displacements presented in the previous section. A co-rotational deformation formulation is used allowing rotation, translation, and distortion, thereby eliminating numerical instability associated with small gauge

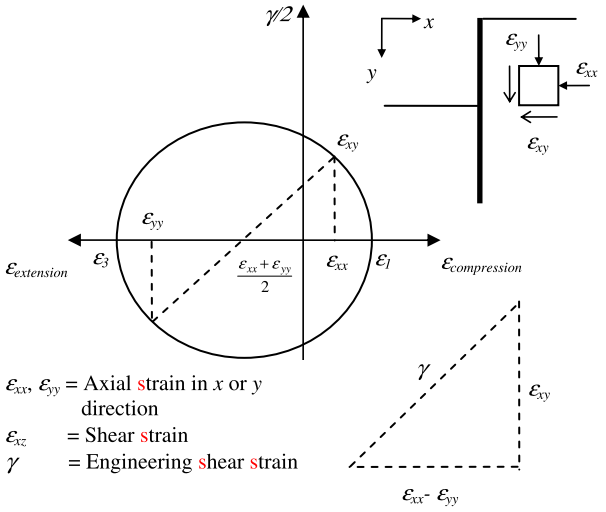

Fig. 17. Mohr's circle of strain.

length and separating the rigid body rotation from the deformation (White et al., 2003).

Strains can be visualized using Mohr's circle of strain shown in Fig. 17. Since the PIV displacement data were obtained from two cameras, it is difficult to obtain a complete strain profile directly from the PIV method. A new strain calculation mesh must be built and the displacement data obtained by linear interpolation. By applying the small strain formulation, all necessary strain components (ε_{xx}, ε_{zz}, and ε_{xz}) can be obtained.

The calculation of strain is highly vulnerable to errors in the displacement data. Errors evolve as a result of the level of accuracy of the PIV and from the difficulties associated with stitching together the PIV data from different cameras. The standard deviation in pixel space for the calibration procedure is about 0.3 pixels, corresponding to an error of 0.1 mm in model scale (6 mm in prototype scale).

14. Engineering shear strain calculation

Engineering shear strain, a total measure of strain in the x–z plane, is a useful quantity in understanding the mechanism of the interaction between the retaining structure and the soil. In plane-strain conditions, shear strain ε_{xz} and engineering shear strain γ can be visualized using Mohr's circle of strain. The engineering shear strain can be calculated from

$$\gamma = \sqrt{(\varepsilon_{xx}-\varepsilon_{zz})^2+(2\varepsilon_{xz})^2} \tag{8}$$

Fig. 18(a)–(c) shows the engineering shear strain on the active side of the wall for excavation depths of 1.08 m, 3.24 m, and 5.40 m in Test 5.

For an excavation depth of 1.08 m, the wall behaved as a simple cantilever; the first layer of props was then introduced and slightly pre-loaded. Due to the increase in lateral stress near the soil surface, some shear strain concentration occurred near the wall crest on the retained side.

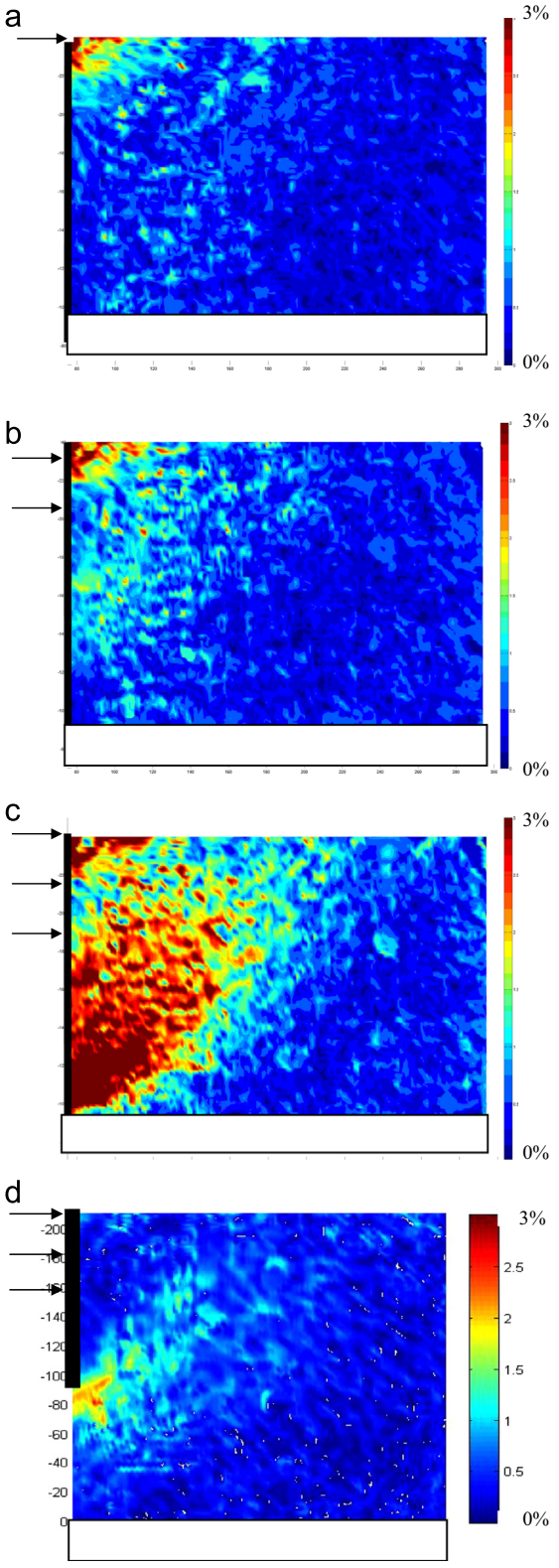

Fig. 18. Engineering shear strain plots on active side for (a) Stage 1, (b) Stage 2 and (c) Stage 3 for Test 5, and (d) Stage 3 for Test 1.

When the excavation depth increased to 3.24 m, the 2nd layer of props was introduced. A shear zone developed near the wall toe as a result of wall rotation about the crest of the retaining wall. The average shear strain level was then about 1%.

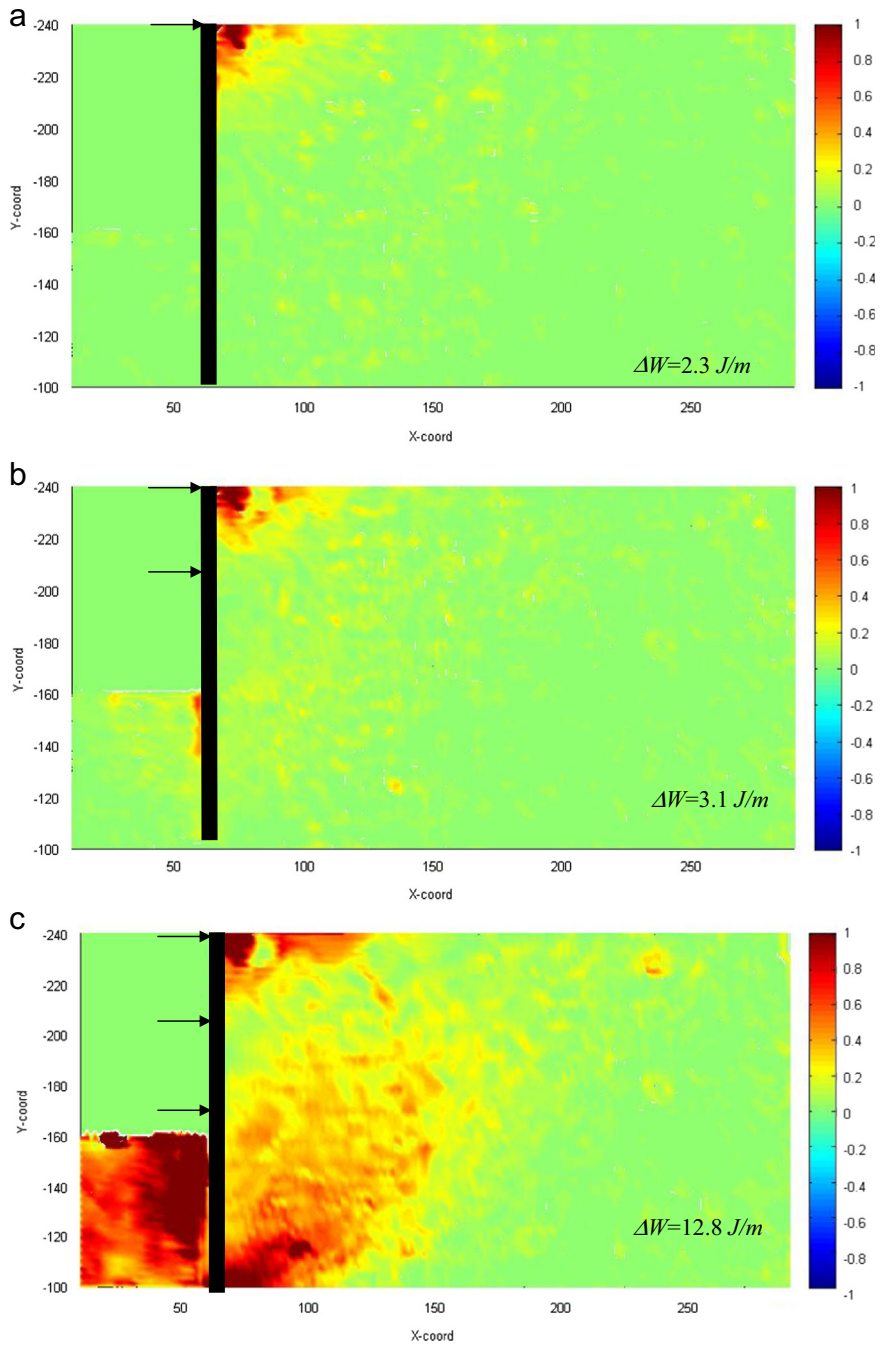

Fig. 19. Work done at excavation depths of (a) 1.08 m, (b) 3.24 m, and (c) 5.40 m for Test 5.

After the installation of the third layer of props, a deep seated soil movement developed. A shear band developed from the wall toe and extended upwards towards the soil surface.

Data from Test 5 (Fig. 18(c)) and Test 1 (Fig. 18(d)) offer the opportunity of examining the difference in mechanism when comparing excavation cases with rigid and flexible walls. With a rigid retaining wall, the wall flexure below the lowest prop location is the main deformation mechanism. A very thin shear band developed at the toe of the wall and extended towards the soil surface. In contrast, around a flexible wall, no soil arch forms as a result of the rigidity of the displacement boundary, suppressing the bulging of the wall.

15. Validation of the energy conservation principle

A simple analytical design framework, known as the Mobilizable Strength Design (MSD) method, was developed by Osman and Bolton (2004). This uses the principle of the conservation of energy within a geo-structural mechanism to predict deformations based on known soil constitutive behavior. Lam and Bolton (2011) used this method to calculate the

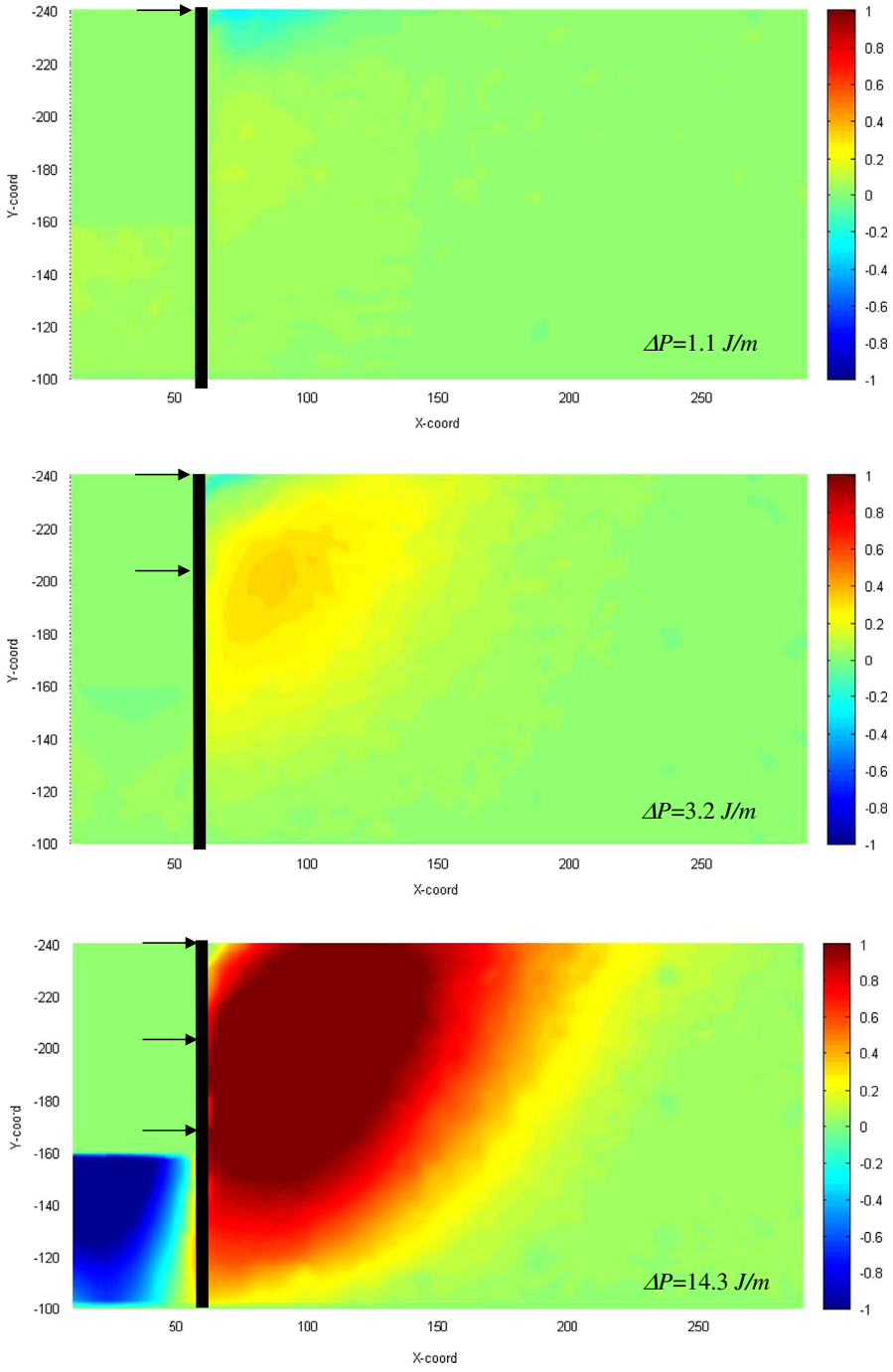

Fig. 20. Potential energy change for excavation depths of 1.08 m, 3.24 m, and 5.40 m for Test 5.

displacement for each excavation stage by considering an admissible deformation mechanism for base heave. The mobilizable shear strength within the mechanism was deduced from the mechanism by the conservation of energy. The work done in shearing the soils was balanced with the change in potential energy of the soil and the structural strain energy stored in the system for each excavation increment. This incremental approach provides a simple tool for deformation assessments. The following analysis validates this design methodology using experimental evidence.

By the conservation of energy for a geo-structural mechanism, following Lam and Bolton (2011), the total loss in potential energy of the soil (ΔP) must balance the total work done in shearing the soil (ΔW) and the total elastic strain energy stored both in bending the wall (ΔU_1) and in compressing the props (ΔU_2).

$$\Delta P = \Delta W + \Delta U_1 + \Delta U_2 \tag{9}$$

The net change in gravitational potential energy (ΔP) is given by the sum of the changes in potential energy for each soil

element, as follows:

$$\Delta P = \sum_{i=1}^{n} \left[\int_{Area} \gamma_{sat}(i) \delta w_y(i)\, dA \right] \tag{10}$$

where $\delta w_y(i)$ is the vertical component of displacement of the soil in the ith soil element and $\gamma_{sat}(i)$ is the saturated unit weight of the soil in the ith soil element.

While calculating the engineering shear strain, soil elements are formed as triangles linking three neighboring patches. The total work done, ΔW, in shearing the soil is given by summing for each element, namely,

$$\Delta W = \sum_{i=1}^{n} \left[\int_{Area} c_{mob}(i) |\delta\gamma(i)|\, dA \right] \tag{11}$$

where $c_u(i)$ is the undrained shear strength of soil in the ith element, $d\gamma(i)$ is the shear strain increment of the soil in the ith element, and the corresponding mobilized strength ratio is given by the stress–strain relation defined by the simple power law derived from Eqs. (4) and (5) using the least squares method.

$$\frac{c_{mob}}{c_u} = (\gamma/\gamma_u)^a \tag{12}$$

where parameters γ_u and a were found to be 5% and 0.33, respectively. The work done per unit area in the element is calculated as the area under the stress strain curve.

The total elastic strain energy stored in the wall, ΔU_1, can be evaluated by repeatedly updating the deflected shape of the wall. It is necessary to do this since U is a quadratic function of displacement.

$$\Delta U_1 = \int_0^s \frac{EI\kappa^2}{2}\, dx = \int_0^s \frac{M^2}{2EI}\, dx \tag{13}$$

where E, I, and κ are the elastic modulus, the second moment of area per unit width of the wall, and the wall curvature, respectively, and s is the length of the wall below the lowest prop.

The total elastic energy stored in the props, ΔU_2, can be estimated by calculating the sum of the product of the displacement of the prop after installation and the maximum prop force at different elevations.

$$\Delta U_2 = \sum_{i=1}^{n} \frac{F_i w_i}{2} \tag{14}$$

where F_i is the maximum prop force after installation and w_i is the corresponding compressive displacement.

Following the strain map created from the PIV data, a work map is calculated. Fig. 19 shows the total work done per meter width (at model scale) in deforming the soil around an excavation in shallow clay using a flexible wall at different stages of excavation. The total work done at different stages is calculated by Eq. (11). On the other hand, the total change in potential energy by the soil elements at different stages is evaluated by Eq. (10) and the distribution is plotted in Fig. 20. The wall bending elastic energy and the prop elastic energy are calculated by Eqs. (13) and (14), respectively. The potential energy change (ΔP) should be equal to the sum of the work done by the shearing of the soil and the elastic energy stored in the retaining structure ($\Delta U_1 + \Delta U_2 + \Delta W$) assuming minimal boundary friction at the interfaces of the solid boundaries and the soil. Except for the first excavation stage of Test 5, the calculated potential energy change is within 25% of the calculated work done on the soil structure system. For the first excavation stage, since the fine measurements of the displacement from the PIV data are prone to errors, due to the calibration of the control markers and photo stitching, the difference between ΔP and $\Delta U_1 + \Delta U_2 + \Delta W$ can be as large as 64%. The variation in the potential energy change and the work done by the soil structure system are plotted in Fig. 21. The difference in the energy terms is less than 30%. Table 4 summarizes the results of the studies of Tests 2, 3, and 5. Results suggested that generally ΔP and $\Delta U_1 + \Delta U_2 + \Delta W$ agree well.

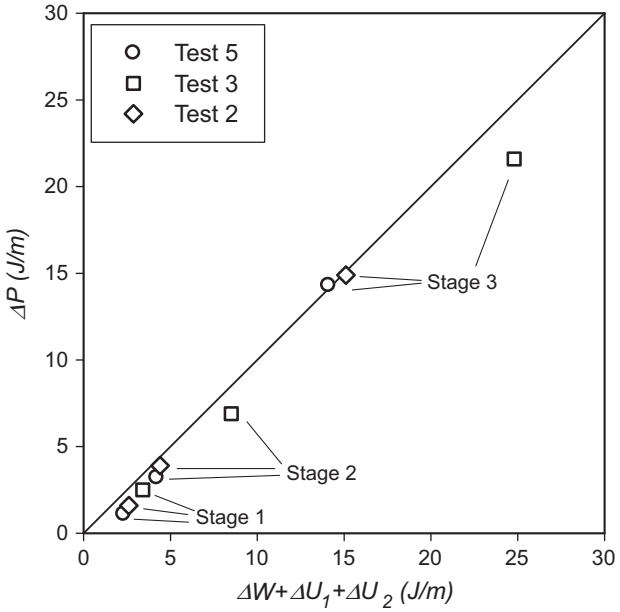

Fig. 21. Potential energy change versus work done on the soil–structure system.

Following the analytical procedures described in Lam and Bolton (2011), predictions of the lateral wall displacement profiles for centrifuge Tests 1 and 2 can be compared with the observations in Fig. 22. The calculations adapt the same undrained strength profiles with the appropriate construction sequences, geometries of the structures and excavation, and small-strain stress–strain relationships described earlier in the paper. The displacement profile typically fell within 30% of the observation in the centrifuge. Although there are discrepancies in the deformation shape, the overall average work done due to plastic flow was correctly approximated. A similar validation of the method carried out by Lam and Bolton (2012) shows predictions within an error of 40% for more than 100 field records. Considering the lack of any detailed account of the soil anisotropy, the performance of the current MSD method is satisfactory.

Table 4
Summary of calculated energy terms for different tests.

Test & stage		ΔU_1 (J/m)	ΔU_2 (J/m)	ΔW (J/m)	$\Delta W+\Delta U_1+\Delta U_2$ (J/m)	ΔP (J/m)	% Error
Test 5	1	0.007	0.03	2.3	2.3	1.1	−52.9
	2	0.98	0.08	3.1	4.2	3.2	−23.1
	3	1.1	0.19	12.8	14.1	14.3	1.49
Test 3	1	0.006	0.08	3.3	3.4	2.5	−34.2
	2	1	0.12	7.4	8.5	6.9	−23.4
	3	0.1	0.17	24.5	24.8	21.6	−12.8
Test 2	1	0.007	0.09	2.5	2.6	1.6	−63.5
	2	1.00	0.12	3.3	4.4	3.9	−12.8
	3	2.4	0.16	12.5	15.1	14.9	−1.06

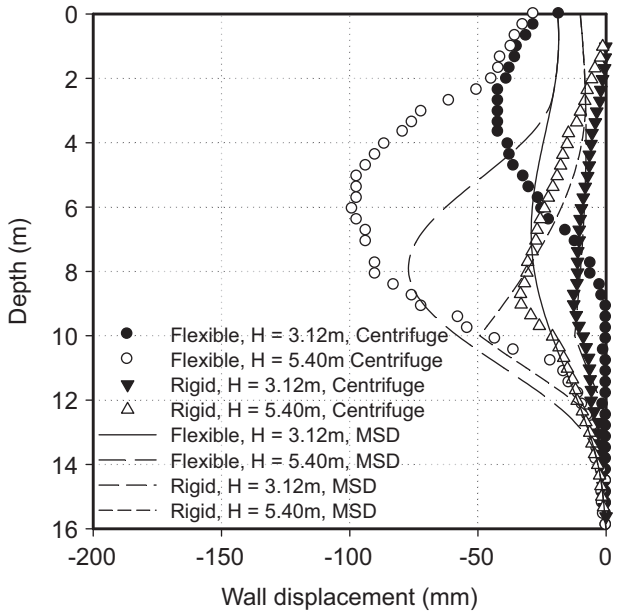

Fig. 22. Predicted and measured lateral wall displacements with depth.

16. Conclusions

With the aid of advanced physical model testing, the performance of various model excavations was monitored. The ground deformation was closely monitored during the in-flight excavation process. Some of the key conclusions are

- The wall deformation profile generally follows the cosine bulge equation proposed by O'Rourke (1993). Averaged soil strains mobilized in the system are below 2%, reiterating the importance of small-strain stiffness for excavation problems.
- The trend lines given by Clough et al. (1989) for estimating wall lateral displacement in relation to factors of safety generally match the observed data. Should improvement on accuracy be desired, engineers may look into the small-strain stiffness of soils, the incremental construction sequence, and most importantly the characteristics of the deformation mechanism.
- In general, the maximum wall displacement is more sensitive to the fixity at the wall toe than to the depth of the clay stratum. The extent of the settlement trough behind the wall, however, is a function of the depth of the clay stratum.
- A reduction in strut stiffness increases wall deflection above the foundation level. The softer prop response induced a shallower local triangular mechanism with a deep, narrow trough near the retaining structures.
- The conservation of energy as a principle for design is validated satisfactorily with experimental evidence. The performance of the MSD method falls within 30% of the centrifuge test measurements.

A simple MSD analysis can be performed within a reasonably short time period, which could be a useful tool in taking key design decisions as a precursor of a site-specific numerical analysis.

References

Bolton, M.D., Lam, S.Y., Osman, A.S., 2008. Supporting Excavations in Clay-Form Analysis to Decision-Making. Special Lecture, 6th International Symposium of Geotechnical Aspects of Underground Construction in Soft Ground, Shanghai.

Clough, G.W., O'Rourke, T.D., 1990. Construction induced movements of in-situ walls. In: Proceedings of Design and Performance of Earth Retaining Structure, ASCE Special Conference, Ithaca, New York, pp. 439–470.

Clough, G.W., Smith, E.W., Sweeney, B.P., 1989. Movement control of excavation support system by iterative design. Foundation Engineering Current Principles and Practices, vol. 2. ASCE, New York, NY869–882.

Haigh, S.K., Madabhushi, S.P.G., 2002. Dynamic centrifuge modeling of the destruction of Sodom and Gomorrah, International conference on physical modeling in geotechnics. St. John's New found land, Canada.

Jamiolkowski, M., Ladd, C.C., Germaine, J.T., Lancellotta, R., 1985. New developments in field and laboratory testing of soils. In: Proceedings of 11th ICSMFE, vol. 1, pp. 57–153.

Jen, L.C., 1998. The Design and Performance of Deep Excavation in Clay (Ph. D. thesis), MIT.

Lam, S.Y., 2010. Ground Movements Due to Excavation in Clay: Physical and Analytical Models (Ph.D. thesis), University of Cambridge.

Lam, S.Y., Bolton, M.D., 2011. Energy conservation as a principle underlying mobilizable strength design for deep excavations. J. Geotech. Geoenviron. Eng., ASCE 137 (11), 1062–1075.

Lam, S.Y., Haigh, S.K., Bolton, M.D., 2011. Understanding ground deformation mechanisms during multi-propped excavation in soft clay. In: Proceedings of the 7th International Symposium on Geotechnical Aspects of Underground Construction in Soft Ground, Rome.

Lam, S.Y., Bolton, M.D., 2012. Energy conservation as a principle underlying mobilizable strength design for deep excavations. J. Geotech. Geoenviron. Eng., ASCE 137, 1062–1075.

Lam, S.Y., Elshafie, M.Z.E.B., Haigh, S.K., Bolton, M.D., 2012. A new apparatus for modelling excavations. Int. J. Phys. Model. Geotech. 12 (1), 24–38.

Leong, E.C., Yeo, S.H., Rahardjo, H., 2005. Measuring shear wave velocity using bender elements. Geotechn. Test. J. 28 (5), 488–498.

Loh, C.K., Tan, T.S., Lee, F.H., 1998. Three dimensional excavation tests in the centrifuge. In: Proceedings of Centrifuge 98, Tokyo.

Madabhushi, S.P.G., Houghton N.E., Haigh S.K., 2006. A new automatic sand pourer for model preparation at University of Cambridge. In: Proceedings of the International Conference of Physical Modeling in Geotechnics, Hong Kong, pp. 217–222.

Mana, A.I., Clough, G.W., 1981. Prediction of movements for braced cuts in clay. ASCE J. Soil Mech. Found. Div. 107 (6), 759–777.

O'Rourke, T.D., 1993. Base stability and ground movement prediction for excavations in soft clay. Retaining Structures. Thomas Telford, London 131–139.

Osman, A.S., Bolton, M.D., 2004. A new design method for retaining walls in clay. Can. Geotech. J. 41 (3), 453–469.

Osman, A.S., Bolton, M.D., 2006. Ground movement predictions for braced excavations in undrained clay. J. Geotech. Geoenviron. Eng., ASCE 132 (4), 465–477.

Powrie, W., 1986. The Behavior of Diaphragm Walls in Clay (Ph.D. thesis), University of Cambridge.

Takemura, J., Kondoh, M., Esaki, T., Kouda, M., Kusakabe, O., 1999. Centrifuge model tests on double propped wall excavation in soft clay. Soils Found. 39 (3), 75–87.

Vardanega, P.J., 2012. Strength Mobilization for Geotechnical Design and its Application to Bored Piles (Ph.D. thesis), University of Cambridge.

Viggiani, G., Atkinson, J.H., 1995. Stiffness of fine-grained soil at very small strains. Geotechnique 45 (2), 249–265.

White, D.J., Take, W.A., Bolton, M.D., 2003. Soil deformation measurement using particle image velocimetry (PIV) and photogrammetry. Geotechnique 53 (7), 619–631.